Distribution of Aerosolized Particles in Healthy and Emphysematous Rat Lungs: Comparison Between Experimental and Numerical Studies

Jessica M. Oakes, Alison Marsden, Céline Grandmont, Chantal Darquenne, Irene Vignon-Clementel

Preprint (published in Journal of Biomechanics) doi:10.1016/j.jbiomech.2015.01.004i

Distribution of Aerosolized Particles in Healthy and Emphysematous Rat Lungs: Comparison Between Experimental and Numerical Studies

Jessica M. Oakes[1,2], Alison L. Marsden[3], Celine Grandmont[1,2], Chantal Darquenne[4], Irene E. Vignon-Clementel[1,2,*]

Abstract

In silico models of airflow and particle deposition in the lungs are increasingly used to determine the therapeutic or toxic effects of inhaled aerosols. While computational methods have advanced significantly, relatively few studies have directly compared model predictions to experimental data. Furthermore, few prior studies have examined the influence of emphysema on particle deposition. In this work we performed airflow and particle simulations to compare numerical predictions to data from our previous aerosol exposure experiments. Employing an image-based 3D rat airway geometry, we first compared steady flow simulations to coupled 3D-0D unsteady simulations in the healthy rat lung. Then, in 3D-0D simulations, the influence of emphysema was investigated by matching disease location to the experimental study. In both the healthy unsteady and steady simulations, good agreement was found between numerical predictions of aerosol delivery and experimental deposition data. However, deposition patterns in the 3D geometry differed between the unsteady and steady cases. On the contrary, satisfactory agreement was not found between the numerical predictions and experimental data for the emphysematous lungs. This indicates that the deposition rate downstream of the 3D geometry is likely proportional to airflow delivery in the healthy lungs, but not in the emphysematous lungs. Including small airway collapse, variations in downstream airway size and tissue properties, and tracking particles throughout expiration may result in a more favorable agreement in future studies.

Keywords: Airflow, Particle deposition, Multi-scale, Aerosol exposure experiments, Computational fluid dynamics

1. Introduction

Computational fluid and particle dynamics simulations provide detailed spatial and temporal distributions of airflow and particles in healthy and diseased lungs. However, to increase confidence in these models, results must be validated against *in vivo* experimental data. While several groups have shown good agreement between three-dimensional (3D) flow (6; 19) and particle-based (14; 15; 16; 35; 32) models with *in vitro* experiments, these comparisons are not sufficient for validation of *in vivo* conditions. While one-dimensional (1D) particle transport models have relatively well predicted *in vivo* data of total and regional deposition in the human (5; 2; 13) and rat lung, (27; 1) they do not provide detailed spatial information. Recently, Minard et al. (17) showed promising agreement between *in silico* predictions and *in vivo* magnetic resonance (MR) derived flow fields in rat lungs. While these previous studies have advanced the validity of computational models, none of them compared multi-scale simulations to regional particle deposition data in both healthy and diseased lungs.

Emphysema, a disease characterized by increased tissue compliance, expanded acinar volume, and decreased small airway diameter compared to normal, (31) has been shown to impact particle deposition in the lungs (20; 30; 4). To study the influence of emphysema-like morphometric changes on particle deposition, we previously (20) employed MR methods (24) to determine lobar deposition in elastase-treated and healthy rat lungs. Results showed, for rats

*Corresponding Author, REO project-team, bat 16, INRIA Paris-Rocquencourt - BP 105, 78153 Le Chesnay Cedex (France), Email: irene.vignon-clementel@inria.fr, Phone: +33-1-39-63-51-18, Fax: +33-1-39-63-58-82

[1]INRIA Paris-Rocquencourt, 78153 Le Chesnay Cedex, France

[2]UPMC Universite Paris 6, Laboratoire Jacques-Louis Lions, 75005 Paris, France

[3]Mechanical and Aerospace Engineering Department, University of California San Diego, La Jolla, CA 92093, USA

[4]Department of Medicine, Division of Physiology, University of California San Diego, La Jolla, CA 92093 USA

ventilated with the same breathing parameters, that particle concentration was higher in the elastase-treated lungs, compared to the healthy lungs. However, the distribution of particles to the lobes was the same in the healthy and emphysematous rats (20) despite the MR and histological measurements suggesting heterogeneous distribution of emphysema-like structures in several lobes of the emphysematous group.

Recently, we developed a 3D-0D coupled numerical model to study airflow and particle deposition in healthy and emphysematous rat lungs (22) that was parameterized from the experimental data of Oakes et al. (20). The goal of the current study was to extend this previous 3D geometric model (23) and to compare regional deposition predictions to experimental data (20). These simulations required matching the numerical model as closely as possible to the experimental conditions and comparing the predicted distribution of inhaled particles to the experimental lobar deposition. Using this *in silico* model, we explored the influence of flow conditions (unsteady versus steady) and initial particle spatial distribution on deposition and lobar delivery.

2. Methods

2.1. Multi-Scale Numerical Airflow Framework

The numerical framework has been previously described in Oakes et al. (22). The 3D geometry was created with a custom version of the open source software, SimVascular (simvascular.org) (28) and includes up to 16 airway generations, with 81 terminal airways (Figure 1) (23). Airflow was simulated with an open source stabilized finite element Navier-Stokes solver, assuming rigid walls and incompressible Newtonian flow (density = 1.2 x 10^{-6} $\frac{g}{mm^3}$, viscosity = 1.81 x 10^{-5} $\frac{g}{mm-s}$). A custom linear solver was employed, incorporating resistance-based preconditioning with a combination of GMRES and conjugate gradient methods (9). Three respiratory cycles were simulated with six Newton iterations of the linear system within each time step of 10^{-4} s. Anisotropic mesh adaptation based on the Hessian of the velocity field was employed to ensure mesh convergence of the solution (18) using meshsim (Simmetrix, Troy NY). Mesh convergence was confirmed for both the flow field and particle deposition.

A no-slip boundary condition was assigned at the airway walls, the experimentally measured time-varying pressure ($P_H(t)$ or $P_E(t)$, H: healthy, E: Emphysema) (22) was applied at the trachea face (Figure 1A) and 0D resistance ($R_{i,j}$) and compliance ($C_{i,j}$) models (3) were implemented at each distal face by implicitly coupling the 0D models to the 3D model (11). A representative healthy and emphysematous rat were chosen to match the rat-specific global parameters with its pressure curve. The 0D model is governed by the following equation:

$$R_{i,j}\frac{dV(t)_{i,j}}{dt} + \frac{V(t)_{i,j}}{C_{i,j}} = P(t)_{i,j} - P_{peep}, \tag{1}$$

where $V_{i,j}$ is the inspired volume, $P(t)_{i,j}$ is the pressure at each distal face and the j and i indices identify the distal faces, with lobe j and assigned airway number i. P_{peep} is the constant pressure of 1 cmH_2O (20). Note that the distal pressure P_D in Figure 1 does not appear in this equation as it describes the evolution of the inspired, not the total, volume (22). To prevent numerical instability a convective stabilization scheme (10) was imposed at all faces with $\beta = 0.1$. The resulting resistance in the 3D geometry was calculated at the time of maximum inspiration ($R_{3D,insp}$) and expiration ($R_{3D,ex}$) by dividing the average pressure drop in the 3D geometry by the flow rate at the trachea.

In the next two paragraphs, the parameters $R_{i,j}$ and $C_{i,j}$ were derived using a combination of the experimental measures and a purely 0D model (e.g. Figure 1 C). With this formulation, it was assumed that the 3D resistance did not influence the average flow repartition in the distal branches of the 3D tree. Therefore, the driving pressures, $P_H(t)$ or $P_E(t)$ (Figure 1 A) remained the relevant $P(t)_{i,j}$ for these solely 0D models. This assumption was tested and its validity is confirmed in the discussion section.

Healthy 0D Parameters

The 0D model parameters for the healthy simulations were defined as:

$$C_{i,j} = \frac{A_{i,j}\alpha_j C_{global}}{A_{T_j}} \tag{2}$$

$$R_{i,j} = \frac{R_{global}A_{T_j}}{\alpha_j A_{i,j}}, \tag{3}$$

where α_j is the volume of each lobe divided by the total volume of the lung derived from imaging data at total lung capacity (23), $A_{i,j}$ is the cross-sectional area of each distal face and $A_{T_j} = \sum_{i=1}^{N_{airway}} A_{i,j}$. The global parameters were set to the values previously determined from the experimental data ($R_{global} = 0.098\ cmH_2O - s - cm^{-3}$, $C_{global} = 0.236\ cm^3 - (cmH_2O)^{-1}$) (22). With these definitions $R_{i,j}$ and $C_{i,j}$ are functions of both the fractional cross-sectional area and experimentally-measured lobar volume fraction α_j. Neglecting the 3D region as explained above, all the distal RC 0D models in parallel are mathematically equivalent to a single global RC 0D model. This is due to the fact that the products $R_{i,j}C_{i,j}$ are all equal, i.e. their relaxation times are the same. Following our previous work (22), the 0D resistance during expiration was set to 1.5 times the 0D resistance during inhalation ($R_{i,j_{ex}} = 1.5R_{i,j}$) (26).

In addition to the unsteady simulations, two steady simulations were performed in which either a constant mean (7408 $\frac{mm^3}{s}$) or maximum (12025 $\frac{mm^3}{s}$) inhalation flow rate was set at the inflow trachea face and $R_{i,j}$ were applied as the outlet boundary conditions at the distal faces.

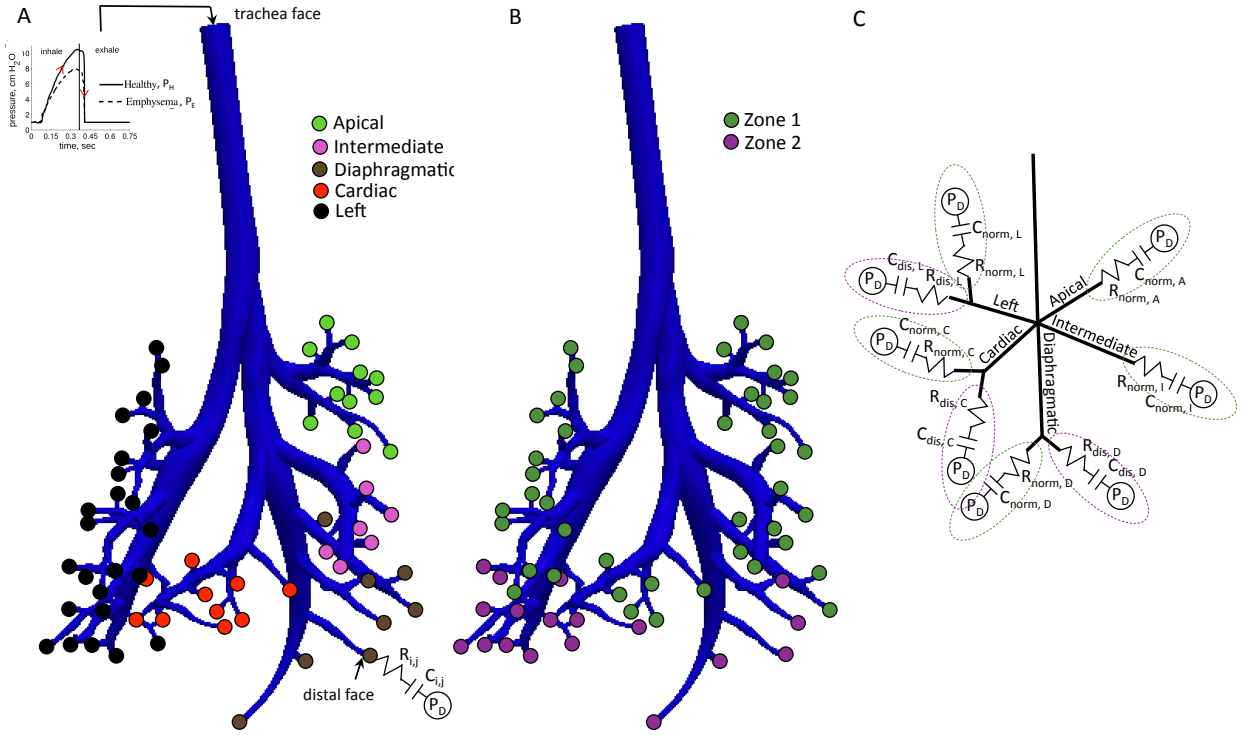

Figure 1: 3D airway geometry (23) used for all the simulations. Panel A: Identification of the airways leading to the five lobes. Panel B and C: Definition of the zones used for the emphysematous simulations. Zone 2 (diseased region) was set to be at the bottom 1/3 of the left, cardiac and diaphragmatic lobes. Zone 1 (normal region) was defined as the top 2/3 of the left, cardiac and diaphragmatic lobes and the entire apical and intermediate lobes. Panel C shows the distribution of the normal (R_{norm} and C_{norm}) and diseased (R_{dis} and C_{dis}) parameters for each zone.

2.2. Emphysema 0D Parameters

Emphysematous regions were heterogeneously located in the lung to match the experiments (20). The lung was divided into normal (Zone 1) and diseased (Zone 2) regions (Figure 1B). Due to this heterogeneity, a new procedure to estimate the distal parameters was designed, based on a purely 0D model. In fact, several RC models in parallel are not mathematically equivalent to a single RC model when the characteristic times, that is, the products $\tau = RC$ are not the same. Within each homogeneous region (normal or diseased) these products are the same by construction. However between regions, this is no longer true, that is, a diseased RC and a normal RC in parallel are no longer formally

equivalent to a global RC model. [Note that only the global compliance, and not the global resistance, changed for the emphysematous rats compared to the healthy rats (22), resulting in different relaxation times between these two states.] As a result, the relationship between experimentally determined global R and C, and lobar or sublobar values is no longer simple. $R_{i,j}$ and $C_{i,j}$ cannot be described as they were for the healthy simulations, inversely, or directly, proportional to the volume and area fractions. However, they can be determined with a 0D model, in which each homogeneous region (normal or diseased) is represented by a single RC model (Figure 1C).

As the airways in Zone 1 are normal, they were assigned the same $R_{i,j}$, $R_{i,j_{ex}}$ and $C_{i,j}$ as in the unsteady healthy simulations. The inspired volumes, V_j, of the two normal lobes were calculated by directly solving:

$$R_{norm_j}\frac{dV_j}{dt} + \frac{V_j}{C_{norm_j}} = P_E(t) - P_{peep}, \tag{4}$$

where $R_{norm_j} = \frac{1}{\sum_{i=1}^{N_j}\frac{1}{R_{i,j}}}$ and $C_{norm_j} = \sum_{i=1}^{N_j} C_{i,j}$. N_j is defined as the total number of airways within Zone 1 of each lobe j.

The total inspired volume $V_{T_{dis}}$ of the three diseased lobes (diaphragmatic, cardiac, and left lobes) were found by subtracting the volume delivered to the apical and intermediate lobe from the total inhaled volume (2.2 mL) (22). The remaining volume was distributed amongst the three diseased lobes with $V_{E_j} = \frac{V_{T_{dis}}\alpha_j}{\sum_{j=1}^{3}\alpha_j}$. For Zone 1 (i.e. the healthy part) of the diseased lobes, V_j was calculated directly with Eqn. 4 for R_{norm_j} and C_{norm_j} of Zone 1 and was subtracted from V_{E_j} to find the total inspired volume of the diseased part of each diseased lobe, $V_{dis,insp_j}$. Then,

$$R_{dis_j}\frac{dV_{dis_j}}{dt} + \frac{V_{dis_j}}{C_{dis_j}} = P_E(t) - P_{peep} \tag{5}$$

was inversely solved and unique R_{dis_j} and C_{dis_j} were found to satisfy $V_{dis_j}(t = t_{insp}) = V_{dis,insp_j}$. $R_{i,j}$ and $C_{i,j}$ of the terminal airways in Zone 2 were then distributed according to:

$$C_{i,j} = \frac{A_{i,j}C_{dis_j}}{A_{T_{dis_j}}} \tag{6}$$

$$R_{i,j} = \frac{R_{dis_j}A_{T_{dis_j}}}{A_{i,j}}, \tag{7}$$

where $A_{T_{dis,j}}$ is the total cross-sectional area of the terminal airways within Zone 2 of each lobe.

2.3. Particle Tracking and Comparison to Experimental Data

Following the airflow simulations, monodisperse inert particles (diameter = $0.95\mu m$, density = $1.35g - cm^{-3}$) were tracked throughout inspiration using Lagrangian methods to solve a reduced form of the Maxey-Riley equation (29; 22). The particles were released at the trachea face throughout inspiration, and the number of particles released was either assigned to be proportional to the local flow rate at the particle starting location (staggered release) or constant in both space and time (uniform release). The gravity vector direction was set to simulate a rat in the supine position. Particles were assumed to have either deposited or exited once they left the 3D geometry at either the airway walls or one of the distal faces, respectively. Particle deposition was checked to be independent of both the time step and number of particles released. The percentage of deposited particles was calculated by normalizing the number of particles deposited by the number of particles inspired. Normalized particle delivery to each lobe was calculated by

$$P_{Del_j} = \frac{\sum_{i=1}^{N_j} N_{exit_{i,j}} + N_{wall_j}}{\sum_{j=1}^{5}(\sum_{i=1}^{N_j} N_{exit_{i,j}} + N_{wall_j})}, \tag{8}$$

where $N_{exit_{i,j}}$ is the number of particles to exit each distal face and N_{wall_j} is the number of particles to deposit on the walls of the airways within lobe j of the 3D geometry. The volume normalized particle delivery, VP_{Del_j}, was calculated for each lobe by

$$VP_{Del_j} = \frac{P_{Del_j}}{\alpha_j}. \tag{9}$$

Both P_{Del_j} and VP_{Del_j} were compared to the experimental values of P_{Dep_j} and VP_{Dep_j}, respectively (20). Note that VP_{Dep_j} was found by normalizing P_{Dep_j} by each rat's α_j found in the experimental study. (20)

3. Results

3.1. Resistance and Compliance Identification

Parameter results are presented in Table 1. R_{dis_j} was smaller and C_{dis_j} was larger in Zone 2 of the emphysematous lungs compared to Zone 2 of the healthy lungs (Table 1). The relaxation time constant, $\tau = RC$, was the same for all lobes in the healthy simulations (Table 1). For the emphysematous simulations, Zone 1 had the same τ as the healthy simulations. However τ in Zone 2 was larger in the emphysematous lungs compared to the healthy lungs (Table 1).

3.2. Multi-scale CFD Simulations

Five mesh adaptions were performed and the fourth mesh ($\sim$ 3 million elements) was used for all simulations. Particle deposition was sensitive and slow to converge with mesh refinement despite there being little difference in the flow field between mesh adaptions. Tuning of $R_{i,j}$ was not necessary, as the difference in inspired volume between the 0D model prediction and the 3D simulation result was only 2%. Additionally, the normalized lobar tidal volume was the same as α_j for the healthy case but not for the emphysematous case (Table 2). The flow distribution was mainly driven by the compliance, as the pressure drop given by $\frac{V_{i,j}}{C_{i,j}}$ of Eqn. 1 was $\sim$10 times greater than the pressure drop given by $R_{i,j}\frac{dV_{i,j}}{dt}$. For Zone 1, the percentage of total flow delivery was less in the emphysematous lungs compared to the healthy lungs (Table 1 and Figure 2). Conversely, the delivery of air to Zone 2 was higher in the emphysematous rats compared to the healthy rats (Table 1 and Figure 2). Zone 2 of the emphysematous simulations took longer to empty, as evident by their slower relaxation rates, τ (Table 1), compared to the same regions of the healthy lung (Figure 2). In the emphysematous simulations the diseased regions finished filling after the normal regions (0.384 s vs 0.360 s).

3.3. Flow Profiles in the 3D Geometry

The velocity profile at the trachea entrance was mainly parabolic throughout inspiration and became biased towards the right lung as the flow approached the main carina (Figure 3). The flow slows down as it travels deeper into the lung (Figure 3), since the total cross-sectional area of the 3D geometry increases with increasing generation. As seen previously (22), the flow patterns were highly dependent on the time-point in the breathing cycle (t=0.091 s and t=0.258 s, same flow rate, Figure 3B) as demonstrated in Figure 3C and E for the healthy case and Figure 3D and F for the emphysematous case.

The main bronchi's cross-sectional area increased along their length (23), which caused an adverse pressure gradient along the main bronchioles (Figure 4). The opposite effect occurred for the terminal airways; the cross sectional area decreased along their length, which created an enhanced pressure drop (Figure 4) and increased flow velocity (Figure 3). The time-averaged resistances in the 3D geometry were larger than predicted by both Poiseuille's model and with Pedley et al.'s (25) correction (Table 3).

Steady vs. Unsteady: Contrary to the unsteady simulations, the normalized lobar flow distribution for the steady simulations did not match the normalized lobar volume, α_j (Table 2). The largest deviation was for the intermediate lobe of the steady mean inflow case, where 25% more flow was delivered than expected based on the assumption that the flow distribution is proportional to the lobar volume. This resulted in higher velocity magnitudes in the airways leading to this lobe, compared to the unsteady simulations at the same time point (Figure 3A vs. Figure 3C and E). The pressure drop in the steady simulation at maximum inhalation was 26% greater than the unsteady simulation (Figure 4A vs B).

	Resistance (R) $\frac{cmH_2O-s}{cm^3}$		Compliance (C) $\frac{cm^3}{cmH_2O}$		$\tau = RC$ s		Cross Sectional Area %		Tidal Volume %	
	Healthy	Emphysema	Healthy	Emphysema	Healthy	Emphysema	Healthy	Emphysema	Healthy	Emphysema
Apical: Zone 1	0.907	0.907	0.0260	0.0260	0.0236	0.0236	12.8	12.8	11.01	8.06
Intermediate: Zone 1	0.739	0.739	0.0319	0.0319	0.0236	0.0236	11.5	11.5	13.52	9.90
Diaphragmatic: Zone 2	1.193	0.762	0.0198	0.0548	0.0236	0.0418	8.03	8.03	8.37	16.41
Diaphragmatic: Zone 1	0.509	0.509	0.0463	0.0463	0.0236	0.0236	18.8	18.8	19.61	14.3
Cardiac: Zone 2	2.70	2.05	0.0209	0.0204	0.0236	0.0418	2.93	2.93	3.68	6.25
Cardiac: Zone 1	1.26	1.26	0.0187	0.0187	0.0236	0.0236	6.28	6.28	7.91	5.78
Left: Zone 2	0.826	0.575	0.0286	0.0727	0.0236	0.0418	13.4	13.4	12.1	21.8
Left: Zone 1	0.420	0.420	0.0562	0.0562	0.0236	0.0236	26.3	26.3	23.8	17.4

Table 1: Total model parameters (R and C) and relaxation times ($\tau = RC$), for each zone of the healthy and emphysematous lungs (Figure 1C), total cross-sectional area of the terminal airways within each zone and the total inhaled volume (tidal volume) to each zone found from the 0D-3D simulations are presented.

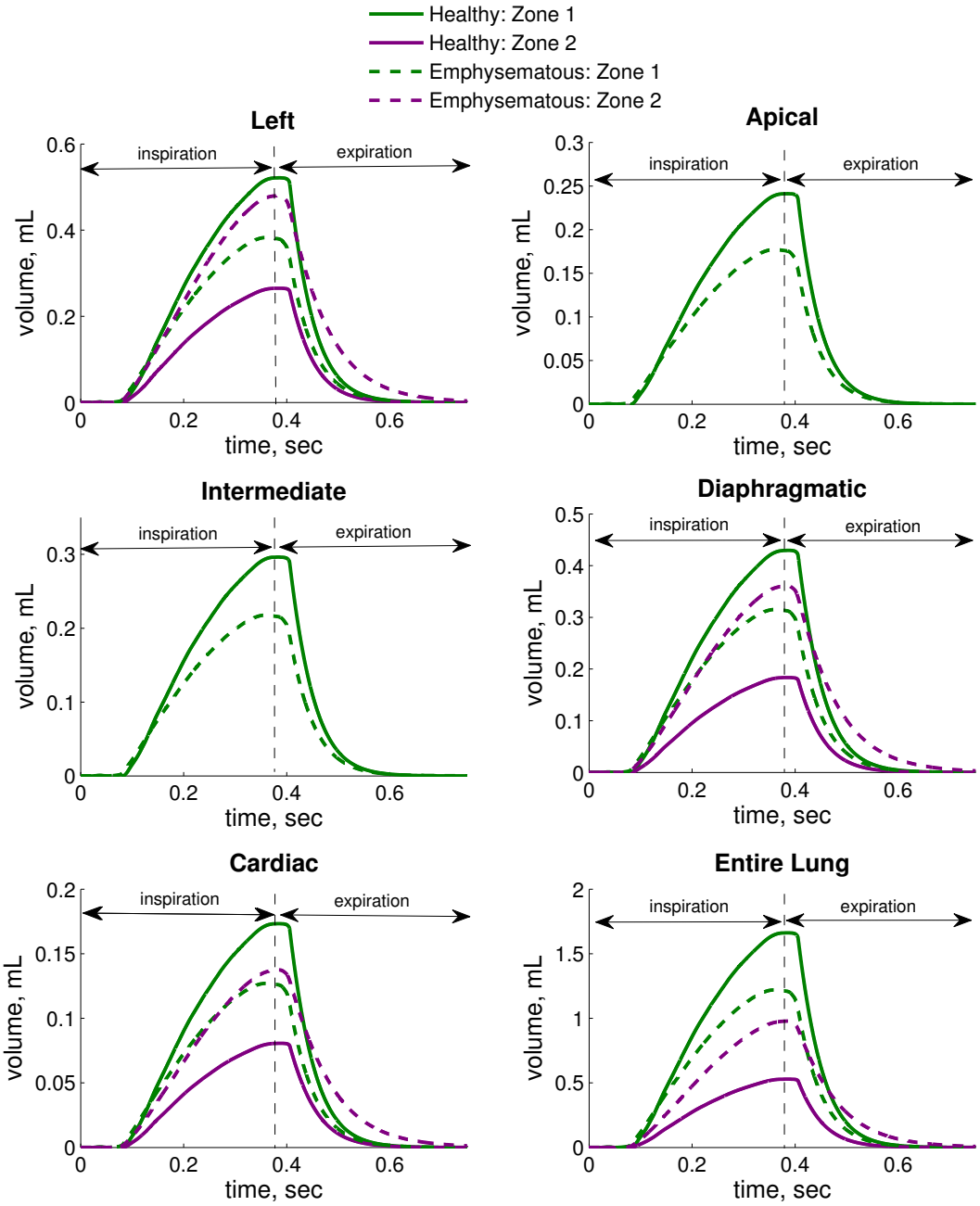

Figure 2: Volume of air entering each zone of each lobe (zone definition is given in Figure 1B) and the total lung (bottom right panel) for the healthy and emphysematous simulations.

Healthy vs. Emphysematous: In the emphysema case, the flow velocities were higher in Zone 2 and lower in Zone 1 compared to the same regions of the healthy simulations (Figure 3D vs C and Figure 3F vs. E). This difference is especially apparent during the deceleration phase of inhalation (Figure 3E and F), likely caused by the airflow phase shift between the two zones in the emphysematous lungs (Figure 2). The flow reverses direction and moves towards the trachea in all the airways at the start of expiration for the healthy simulation (Figure 3B and Figure 3G)). However, in the emphysematous simulation, the air is both moving away (Zone 2) and towards (Zone 1) the trachea at the start

	Subtending Lobe Volume, $\alpha_j * 100$	Healthy Unsteady Tidal Volume, %	Steady: Mean Flow, %	Steady: Maximum Flow, %	Emphysema Tidal Volume, %
Apical	11.0	11.0	11.9	11.1	8.06
Intermediate	13.5	13.5	18.1	14.2	9.90
Diaphragmatic	28.0	28.0	27.9	26.8	30.7
Cardiac	11.6	11.6	10.4	11.4	12.0
Left	35.9	35.9	31.7	36.4	39.2

Table 2: Subtending lobe volume percentage (α_j) (23), inhaled percent lobar volume for the unsteady simulations, and percent lobar flow division for the two steady simulations.

of expiration (Figure 3H), creating asynchrony between the two regions.

While the pressure drop in the 3D geometry is quite similar at maximum inhalation (Figure 4 A and D), the average pressure drop during peak exhalation in the emphysematous lungs was 36% of the pressure drop in the healthy lungs (Figure 4 F vs C). The maximum 3D resistance in the 3D geometry was smaller in the emphysematous simulations compared to the healthy simulation for both inspiration and expiration (Table 3). However, the time-averaged 3D resistance was nearly the same (Table 3) between the two simulations.

3.4. Particle Deposition in the 3D Geometry

There was negligible difference in total particle deposition between the healthy (2.82%) and emphysematous (2.98%) simulations. Similar to our previous study (22), particles deposited mainly at the bifurcation zones and backside (in the direction of gravity) of the 3D geometry (Figure 5) for both the healthy and emphysematous simulations. The relative difference in the percentage of deposited particles in the uniform seeding was 1.5% of the staggered release. Deposition in the 3D geometry was 6.0% less and 6.6% greater than the unsteady simulations for the mean and maximum steady simulations, respectively. Additionally, while the particle deposition sites were spread out in the unsteady simulations, particles tended to pile up in the steady simulations, creating regions of higher particle concentration (Figure 5C and D).

The distribution of deposition in the 3D geometry was impacted by the disease (Figure 6A). The percentage of particles depositing on the airway walls was higher in Zone 2 and lower in Zone 1 in emphysema compared to the healthy simulations (Figure 6A). The concentration of deposited particles was highest in the apical lobe, compared to the other four lobes (Figure 6B) for both the healthy and emphysematous simulations. Particle concentration in Zone 2 was higher in the emphysematous than in the healthy simulations (Figure 6B). Figure 6C shows that the apical lobe had the greatest and the intermediate lobe the smallest number of particles depositing on the wall, when normalized by the flow rate percentage, for both the healthy and emphysematous simulations.

3.5. Particle Distribution: Comparison to Experimental Deposition

There was excellent agreement between the experimental deposition data, P_{Dep}, and the simulated lobar delivery, P_{Del}, for the steady and unsteady healthy simulations (Figure 7A). P_{Del} was slightly lower and slightly higher than P_{Dep} for the apical and cardiac lobes, respectively. While there was no statistical difference (t-test, p>0.5) between VP_{Dep} and VP_{Del}, VP_{Dep} was greater than 1 for the apical and intermediate lobe.

The distribution of particle delivery to the 5 lobes was highly dependent on the seeding profile (Figure 7A); uniform seeding overestimated P_{Del} to the left lobe and underestimated P_{Del} to the diaphragmatic lobes compared to P_{Dep} (Figure 7A).

For the three diseased lobes, good agreement was found between P_{Del} and P_{Dep} for the emphysematous simulations (Figure 7B). VP_{Del} of particles in the emphysematous simulations (Figure 7D) matched VP_{Dep} for only the

	Inspiration		Expiration	
	Maximum	Time-Averaged	Maximum	Time-Averaged
Healthy 0D-3D Simulation	0.087	0.020 ± 0.010	0.196	0.024 ± 0.014
Emp. 0D-3D Simulation	0.056	0.021 ± 0.007	0.061	0.024 ± 0.009
0D (22)	–	0.098	–	0.147
Poiseuille	0.003	0.003	0.003	0.003
Pedley's Correction (25)	–	0.007	–	–

Table 3: Resistance ($\frac{cmH_2O\,s}{cm^3}$) in the 3D geometry calculated from pressure drop found from the 0D-3D simulations and from empirical formulas. Maximum and time-averaged simulated resistances were calculated by taking the mean pressure drop from the trachea to each of the distal faces and by dividing it by the flow rate at the trachea. Resistances calculated with either Poiseuille ($R_p = \frac{8\mu l}{\pi r^4}$, where l and r are the length and radius of the airway, respectively) or Pedley et al.'s correction (25) ($R_{ped} = \frac{1.85R_p}{4\sqrt{2}}\sqrt{\frac{Re2r}{l}}$, where Re is the Reynolds number) were done so by systematically summing up the resistance in each airway by moving from the most distal regions of the tree towards the trachea.

diaphragmatic and cardiac lobes; volume normalized delivery was overestimated in the left lobe and underestimated in the apical and intermediate lobes.

4. Discussion

The goal of this current study was to compare simulated particle delivery in healthy and emphysematous lungs to *in vivo* experimental data. To do this, 3D-0D *in silico* models were created to represent the experimental conditions. Favorable agreement was found for the healthy simulations, however, as the peripheral deposition efficiency differs between diseased and healthy regions of the lung, similar agreement was not found for the emphysematous lungs.

4.1. Particle Deposition and Distribution

4.1.1. Steady vs Unsteady Simulations

Despite steady and unsteady simulations velocity differences (Figure 3), both reasonably predicted the healthy experimental particle lobar distribution (Figure 7A). This finding suggests that if only lobar particle delivery is needed and there is little influence of inertia on the particle transport, then steady simulations may be appropriate. However, if one aims to predict locations of high particle concentration, then steady simulations may not be sufficient (Figure 5).

4.1.2. Staggered vs. Uniform Release

There was good agreement between the experimental deposition and the particle delivery to the lobes for the staggered release, but not for uniform release (Figure 7A). In the latter, the number of released particles was uniform throughout inspiration, independent of the particle's starting location. Slow and fast streamlines carried the same number of particles, causing an unrealistically high (left lobe) or low (diaphragmatic lobe) delivery to areas of the lung which they fed. However, the 3D deposition number was relatively unaffected by this seeding density profile. The staggered release best represents the exposure experiments: a long tube led to the trachea (20), causing particles to convect with the fully developed flow. In agreement with previous work (35), particle distribution in the lung is sensitive to the seeding method and therefore care should be taken when choosing how to initially distribute the particles.

4.1.3. Influence of Airway Geometry

While not statistically different than unity (20), VP_{Dep} in the apical lobe tended to be larger than predicted by α_j for the healthy case (Figure 7C). Since the simulated apical VP_{Del} was close to unity (Figure 7C), lobar ventilation or geometric differences may explain this enhanced deposition. The apical ventilation may be greater than assumed by α_j, resulting in increased particle delivery and thus deposition. Deposition efficiency could also be greater since the apical lobe exhibits dichotomous branching characteristics, while the other lobes branch monopodially (23). Indeed, the apical short branching structure and high surface area to volume characteristics caused enhanced deposition in this 3D region (Figure 6B). The apical lobe also has a shorter path length to the acinus than the other lobes (34), which may result in a higher particle concentration delivery to the acinus and therefore enhanced deposition in this region. The opposite was found for the intermediate lobe, where the branching structure is highly monopodial.

As particles are transported by convection in the conducting airways fewer particles were delivered to lower flow areas. However, lower velocity also means more time to sediment and deposit on the wall. For example, in the diseased cardiac lobe, flow rate and particle delivery increased in emphysema, but particle deposition was higher in the healthy simulations (Figure 6C). The opposite effect was seen for the diaphragmatic lobe (Figure 6C).

4.1.4. Particle Deposition in Emphysema

Experimental total deposition was higher in emphysema. However, these results were not replicated computationally: total 3D deposition was not influenced by the heterogeneous disease. As this 3D geometry only consists of about 4% (23) of total lung volume, this enhanced deposition may occur downstream of the considered geometry, or during expiration. Furthermore, even though there was asynchrony in the filling and emptying of the lobes in the emphysematous simulations (Figure 3H), this only occurred for a short period of the respiration cycle. It is possible that this asynchrony becomes more significant as the disease progresses, causing air to be trapped. Particles suspended in this trapped air will likely have time to sediment and deposit. This failure to flush out potentially harmful particles could contribute to accelerated disease progression.

The numerical simulations were unable to fully reproduce the emphysema P_{Dep} (Figure 7B and D). Particle delivery was not proportional to lobar volume in the emphysema case (Figure 7D). While measured lobar volume was similar between healthy and emphysematous rats (20), computed airflow and hence particle delivery were enhanced in the diseased regions because of their higher compliance. As the inspired air volume distribution no longer followed the lobar volume fraction, lobar particle delivery was no longer proportional to α_j in contrast to the healthy rat case (Figure 7D vs C).

Deposition efficiency in diseased and healthy regions are likely to be different with less deposition occurring in the large acinar airspaces of the diseased lung parenchyma (31; 21). However, reduced traction of the emphysematous tissues on the adjacent small airways decrease their size, potentially increasing small airway deposition. Additionally, small emphysema airways are prone to collapse, (33) likely causing local particle trapping, enhancing sedimentation. But, flow is slower in normal regions (Figure 3), potentially favoring sedimentation in these regions. These contradicting effects make it difficult to predict the behavior of particles downstream of the 3D model and should be examined in future simulations.

5. Limitations

Constant $R_{i,j}$, $R_{i,j_{ex}}$ and $C_{i,j}$ values were used for the 0D model parameters, even though they most likely change throughout inhalation and exhalation. However, it was not possible to define time varying $R_{i,j}$, $R_{i,j_{ex}}$ and $C_{i,j}$, as only constant R_{global} and C_{global} could be found from the experimental data (22). As the particles exhibited little inertia, it is unlikely time varying $R_{i,j}$ and $C_{i,j}$ parameters would impact the particle distribution to the lobes.

While measured experimentally with MRI, (20) there is some uncertainty in the uniformity and location of the disease in the emphysematous lungs. Simulations would benefit from more detailed knowledge of disease location, perhaps measured experimentally by ventilation (12; 8), tissue compliance or sub lobar volumes. While regional ventilation maps in elastase-treated rat lungs (7) exist, it is difficult to apply them to numerical simulations, although (sub-)lobar information would be highly valuable in parameterizing multi-scale simulations.

6. Conclusions

This study was the first to compare 3D numerical particle deposition simulations to experimental data in both healthy and diseased conditions. While both the steady and unsteady simulations reasonably predicted the lobar distribution of particles in the healthy case, the deposition patterns in the 3D geometry was quite different between the two. This finding indicates that if only lobar distribution is needed, steady simulations may be appropriate for the flow and particle properties considered in this study. However, unless the flow delivery to each lung region is known beforehand, emphysema can only be modeled using the unsteady multi-scale techniques employed in the current study. Unlike for the healthy simulations, we were unable to match the emphysema experimental data. This was likely because the airways and pulmonary region downstream of the 3D geometry were lumped in the RC models. In the healthy simulations, it is possible that deposition efficiency downstream of the 3D geometry is relatively similar between lobes. However, in emphysematous lungs, where normal regions are neighboring diseased regions, the deposition efficiency is likely not the same between these different areas of the lung. Therefore factors such as enhanced deposition in the normal acinus regions compared to the diseased regions, smaller airway diameters in diseased regions compared to normal regions, airway collapse in diseased regions, and particle transport through expiration, may impact deposition efficiency downstream of the 3D geometry considered in this study.

Conflict of interest

The authors have no conflict of interest related to the work presented in this manuscript.

Acknowledgments

Chantal Darquenne was supported in part by grant 1R21HL087805-02 from the NHLBI (NIH), Alison L. Marsden was supported in part by an NSF CAREER award and the Burroughs Wellcome Fund Career Award at the Scientific Interface, Jessica M. Oakes was fully supported by the Whitaker International Program administered by the International Institute of Education, and Celine Grandmont was partially supported by the ANR-08-JCJC-0013 and ANR-11-TECS-0006 grants. An associated team INRIA grant covered visit costs for joint work of the co-authors. The authors would like to thank Shawn Shadden for sharing his expertise in particle tracking.

[1] Anjilvel, S. and Asgharian, B., 1995. A multiple path model of particle deposition in the rat lung. Fundamental and Applied Toxicology 28, 41–50.

[2] Asgharian, B., Price, O. T., and Hofmann, W., 2006. Prediction of particle deposition in the human lung using realistic models of lung ventilation. Journal of Aerosol Science 37, 1209–1221.

[3] Bates, J. H. T. and Suki, B., 2008. Assessment of peripheral lung mechanics. Respiratory Physiology & Neurobiology 163, 54–63.

[4] Brand, P., Schulte, M., Wencker, M., Herpich, C. H., Klein, G., Hanna, K., and Meyer, T., 2009. Lung deposition of inhaled alpha1-proteinase inhibitor in cystic fibrosis and alpha1-antitrypsin deficiency. The European Respiratory Journal 34, 354–60.

[5] Darquenne, C. and Paiva, M., 1994. One-dimensional simulation of aerosol transport and deposition in the human lung. Journal of applied physiology 77, 2889–98.

[6] de Rochefort, L., Vial, L., Fodil, R., Maître, X., Louis, B., Isabey, D., Caillibotte, G., Thiriet, M., Bittoun, J., Durand, E., and Sbirlea-Apiou, G., 2007. In vitro validation of computational fluid dynamic simulation in human proximal airways with hyperpolarized 3He magnetic resonance phase-contrast velocimetry. Journal of Applied Physiology 102, 2012–23.

[7] Emami, K., Cadman, R. V., Woodburn, J. M., Fischer, M. C., Kadlecek, S. J., Zhu, J., Pickup, S., Guyer, R. a., Law, M., Vahdat, V., Friscia, M. E., Ishii, M., Yu, J., Gefter, W. B., Shrager, J. B., and Rizi, R. R., 2008. Early changes of lung function and structure in an elastase model of emphysema–a hyperpolarized 3He MRI study. Journal of Applied Physiology 104, 773–786.

[8] Emami, K., Chia, E., Kadlecek, S., Macduffie-Woodburn, J. P., Zhu, J., Pickup, S., Blum, A., Ishii, M., and Rizi, R. R., 2011. Regional correlation of emphysematous changes in lung function and structure: a comparison between pulmonary function testing and hyperpolarized MRI metrics. Journal of Applied Physiology 110, 225–35.

[9] Esmaily Moghadam, M., Basikevs, Y., and Marsden, A. L., 2013. A new preconditioning technique for implicitly coupled multidomain simulations with applications to hemodynamics. Computational Mechanics 52, 1141–1152.

[10] Esmaily Moghadam, M., Bazilevs, Y., Hsia, T.-Y., Vignon-Clementel, I. E., and Marsden, A. L., 2011. A comparison of outlet boundary treatments for prevention of backflow divergence with relevance to blood flow simulations. Computational Mechanics 48, 277–291.

[11] Esmaily Moghadam, M., Vignon-Clementel, I. E., Figliola, R., and Marsden, A. L., 2013. A modular numerical method for implicit 0D/3D coupling in cardiovascular finite element simulations. Journal of Computational Physics 244, 63–79.

[12] Jacob, R. E., Carson, J. P., Thomas, M., and Einstein, D. R., 2013. Dynamic multiscale boundary conditions for 4D CT of healthy and emphysematous rats. PloS one 8, e65874.

[13] Katz, I., Pichelin, M., Caillibotte, G., Montesantos, S., Majoral, C., Martonen, T., Fleming, J., Bennett, M., and Conway, J., 2013. Controlled parametric individualized 2D and 3D imaging measurements of aerosol deposition in the respiratory tract of healthy human subjects preliminary comparisons with simulations. Aerosol Science & Technology 47, 714–723.

[14] Longest, P. W., Tian, G., Walenga, R. L., and Hindle, M., 2012. Comparing MDI and DPI aerosol deposition using in vitro experiments and a new stochastic individual path (SIP) model of the conducting airways. Pharmaceutical Research 29, 1670–88.
[15] Ma, B. and Lutchen, K. R., 2009. CFD simulation of aerosol deposition in an anatomically based human large-medium airway model. Annals of Biomedical Engineering 37, 271–85.
[16] Ma, B., Ruwet, V., Corieri, P., Theunissen, R., Riethmuller, M., and Darquenne, C., 2009. CFD Simulation and Experimental Validation of Fluid Flow and Particle Transport in a Model of Alveolated Airways. Journal of Aerosol Science 40, 403–141.
[17] Minard, K. R., Kuprat, A. P., Kabilan, S., Jacob, R. E., Einstein, D. R., Carson, J. P., and Corley, R. A., 2012. Phase-contrast MRI and CFD modeling of apparent (3)He gas flow in rat pulmonary airways. Journal of Magnetic Resonance 221, 129–138.
[18] Müller, J., Sahni, O., Li, X., Jansen, K. E., Shephard, M. S., and Taylor, C. a., 2005. Anisotropic adaptive finite element method for modelling blood flow. Computer Methods in Biomechanics and Biomedical Engineering 8, 295–305.
[19] Mylavarapu, G., Murugappan, S., Mihaescu, M., Kalra, M., Khosla, S., and Gutmark, E., 2009. Validation of computational fluid dynamics methodology used for human upper airway flow simulations. Journal of Biomechanics 42, 1553–1559.
[20] Oakes, J. M., Breen, E., Scadeng, M., Tchantchou, G. S., and Darquenne, C., 2014. MRI-based measurements of aerosol deposition in the lung of healthy and elastase-treated rats. Journal of Applied Physiology 116, 1561–1568.
[21] Oakes, J. M., Day, S., Weinstein, S. J., and Robinson, R. J., 2010. Flow field analysis in expanding healthy and emphysematous alveolar models using particle image velocimetry. Journal of Biomechanical Engineering 132, 021008–1–9.
[22] Oakes, J. M., Marsden, A. L., Grandmont, C., Shadden, S. C., Darquenne, C., and Vignon-Clementel, I. E., 2014. Airflow and particle deposition simulations in health and emphysema: from in vivo to in silico animal experiments. Annals of Biomedical Engineering 42, 899–914.
[23] Oakes, J. M., Scadeng, M., Breen, E. C., Marsden, A. L., and Darquenne, C., 2012. Rat airway morhometry measured from in-situ MRI-based geometric models. Journal of Applied Physiology 112, 1921–1931.
[24] Oakes, J. M., Scadeng, M., Breen, E. C., Prisk, G. K., and Darquenne, C., 2013. Regional Distribution of Aerosol Deposition in Rat Lungs Using Magnetic Resonance Imaging. Annals of Biomedical Engineering 41, 967–978.
[25] Pedley, T. J., Schroter, R. C., and Sudlow, M. F., 1970. The prediction of pressure drop and variation of resistance within the human bronchial airways. Respiration Physiology 9, 387–405.
[26] Rubini, A., Carniel, E. L., Parmagnani, A., and Natali, A. N., 2011. Flow and volume dependence of rat airway resistance during constant flow inflation and deflation. Lung 189, 511–8.
[27] Schmid, O., Bolle, I., Harder, V., Karg, E., Takenaka, S., Schulz, H., and Ferron, G. A., 2008. Model for the deposition of aerosol particles in the respiratory tract of the rat. I. Nonhygroscopic particle deposition. Journal of Aerosol Medicine and Pulmonary Drug Delivery 21, 291–307.
[28] Schmidt, J. P., Delp, S. L., Sherman, M. A., Taylor, C. A., Pande, V. S., and Altman, R. B., 2008. The Simbios National Center: Systems Biology in Motion. Proceedings IEEE Inst Elect Electron Eng. 96, 1266–1280.
[29] Shadden, S. C. (2010) FlowVC (Version 1) [Computer software]. Retrieved from http://shaddenlab.berkeley.edu/software/.
[30] Sweeney, T. D., Brain, J. D., Leavitt, S. a., and Godleski, J. J., 1987. Emphysema alters the deposition pattern of inhaled particles in hamsters. The American journal of Pathology 128, 19–28.
[31] Thurlbeck, W. M. and Muller, N. L., 1994. Emphysema: Definition, Imaging, and Quantification. American Journal of Roentgenology 163, 1017–1025.
[32] van Ertbruggen, C., Corieri, P., Theunissen, R., Riethmuller, M. L., and Darquenne, C., 2009. Validation of CFD Predictions of Flow in a 3D Alveolated Bend with Experimental Data. Journal of Biomechanics 41, 399–405.
[33] Wright, R. R., 1960. Bronchial atrophy and collapse in chronic obstructive pulmonary emphysema. American Journal of Pathology 37, 63–77.
[34] Yeh, H. C., Schum, G. M., and Duggan, M. T., 1979. Anatomic models of the tracheobronchial and pulmonary regions of the rat. The Anatomical Record 195, 483–92.
[35] Zhang, Z. and Kleinstreuer, C., 2001. Effect of particle inlet distribution in a triple bifurcation lung airway model. Journal of Aerosol Medicine 14, 13–29.

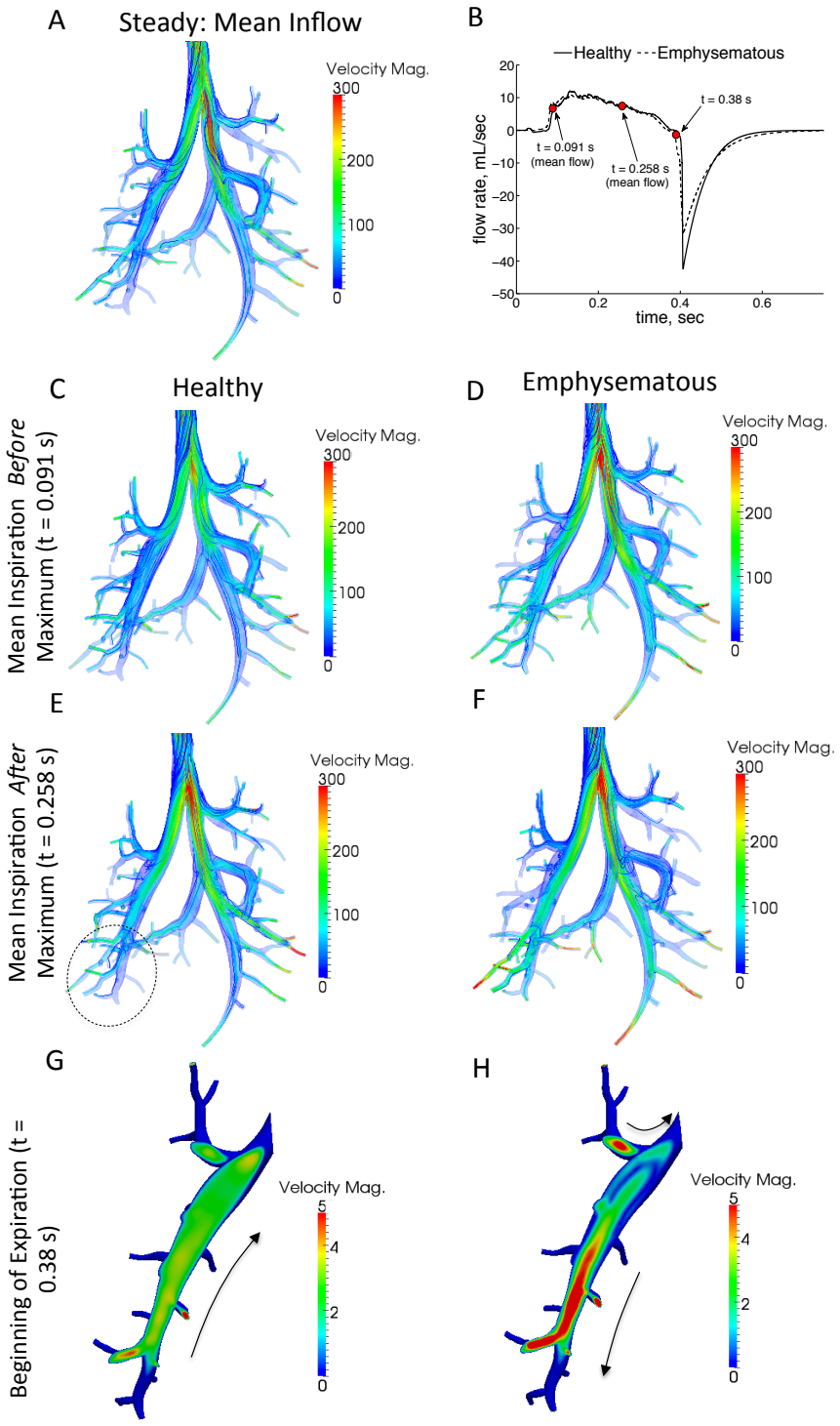

Figure 3: Velocity magnitudes and streamlines ($\frac{cm}{s}$) for the mean inflow steady simulation (A) and the unsteady healthy and emphysematous simulations at the time of mean inspiration before and after the time of maximum inhalation (Healthy: panels C and E, Emphysematous: panels D and F). For visualization purposes the top portion of the trachea is removed in the figure. The velocity magnitude of the bottom part of the left lung (for location see panel E) at the end of inhalation is shown for the healthy (G) and emphysematous (H) simulations. The same phenomenon occurs at the intersection of Zone 2 and Zone 1 in the cardiac and diaphragmatic lobes. Arrows show the general flow direction. The time points where the flow field was plotted for each panel is shown in panel B.

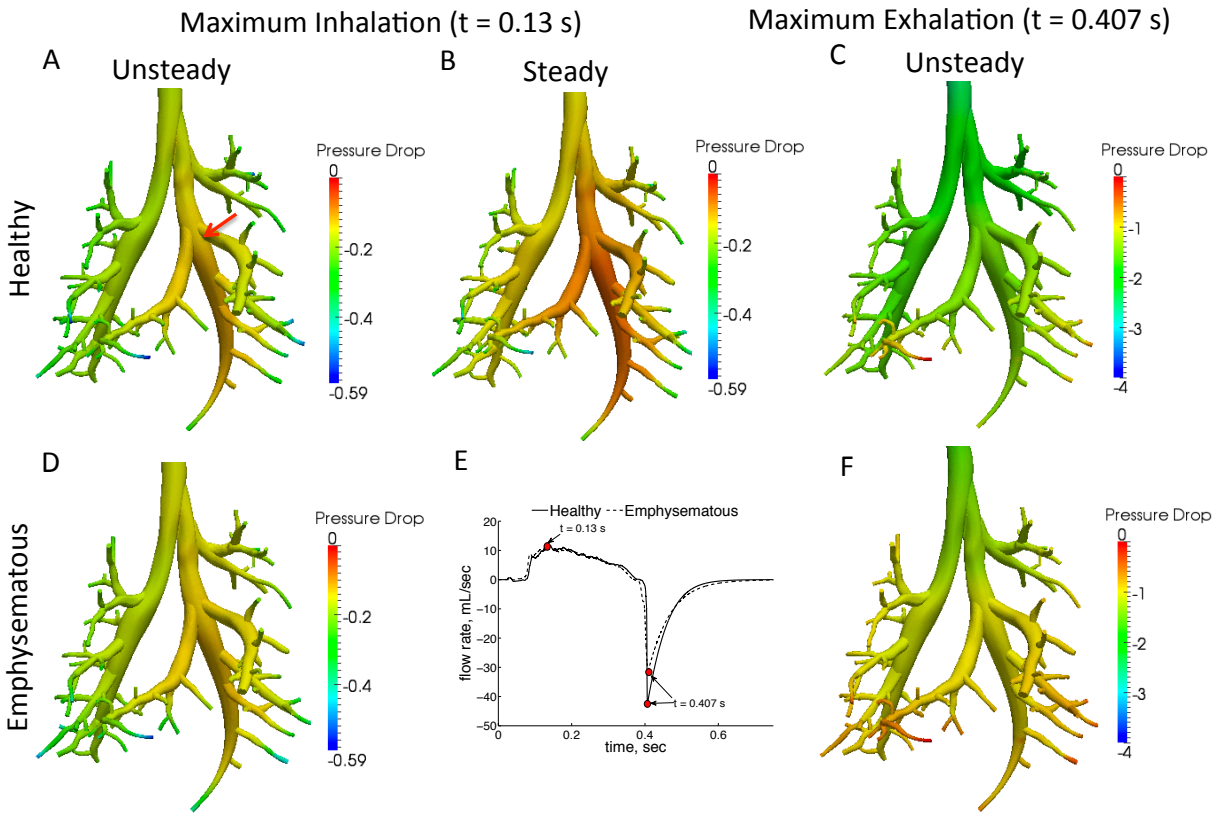

Figure 4: Pressure drop in the 3D geometry (cmH_2O) at maximum inhalation (panels A and D) and maximum exhalation (panels C and F) for the healthy and emphysematous simulations. The red arrow on Panel A shows one of the areas where there was an adverse pressure gradient caused by the increasing diameter of the bronchi. Panel B shows the pressure drop for the steady simulation when the maximum flow rate was prescribed at the trachea face. The pressure drop was calculated by subtracting the 3D pressure by the mean pressure at the trachea or most distal airway for the inspiration and expiration panels, respectively. Panel E shows the time points where the pressure plots were taken.

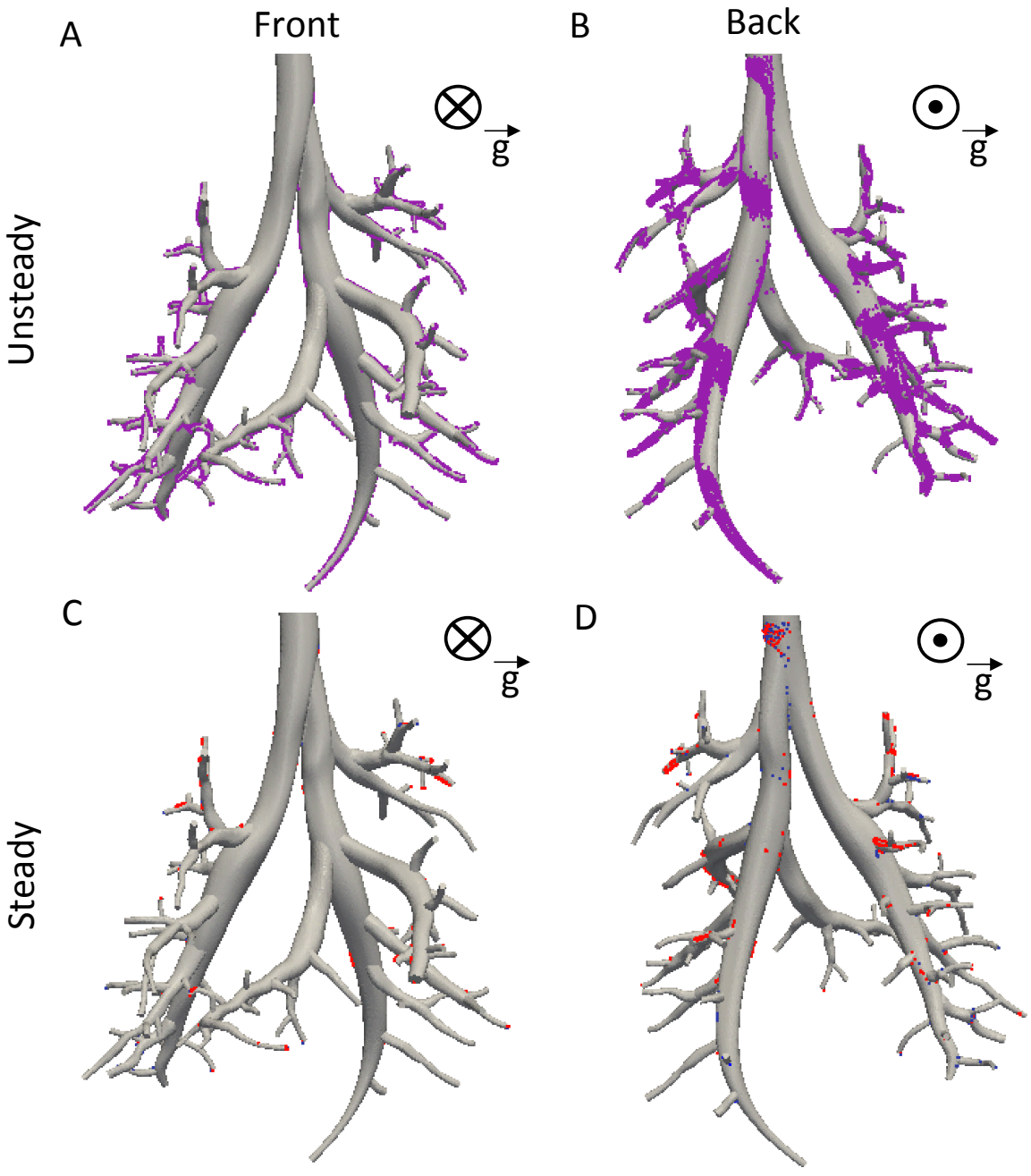

Figure 5: Particle deposition locations for the unsteady healthy (panels A and B) and steady simulations (panels C and D). For the steady simulations, blue and red particles were used for the mean and maximum flow rate, respectively.

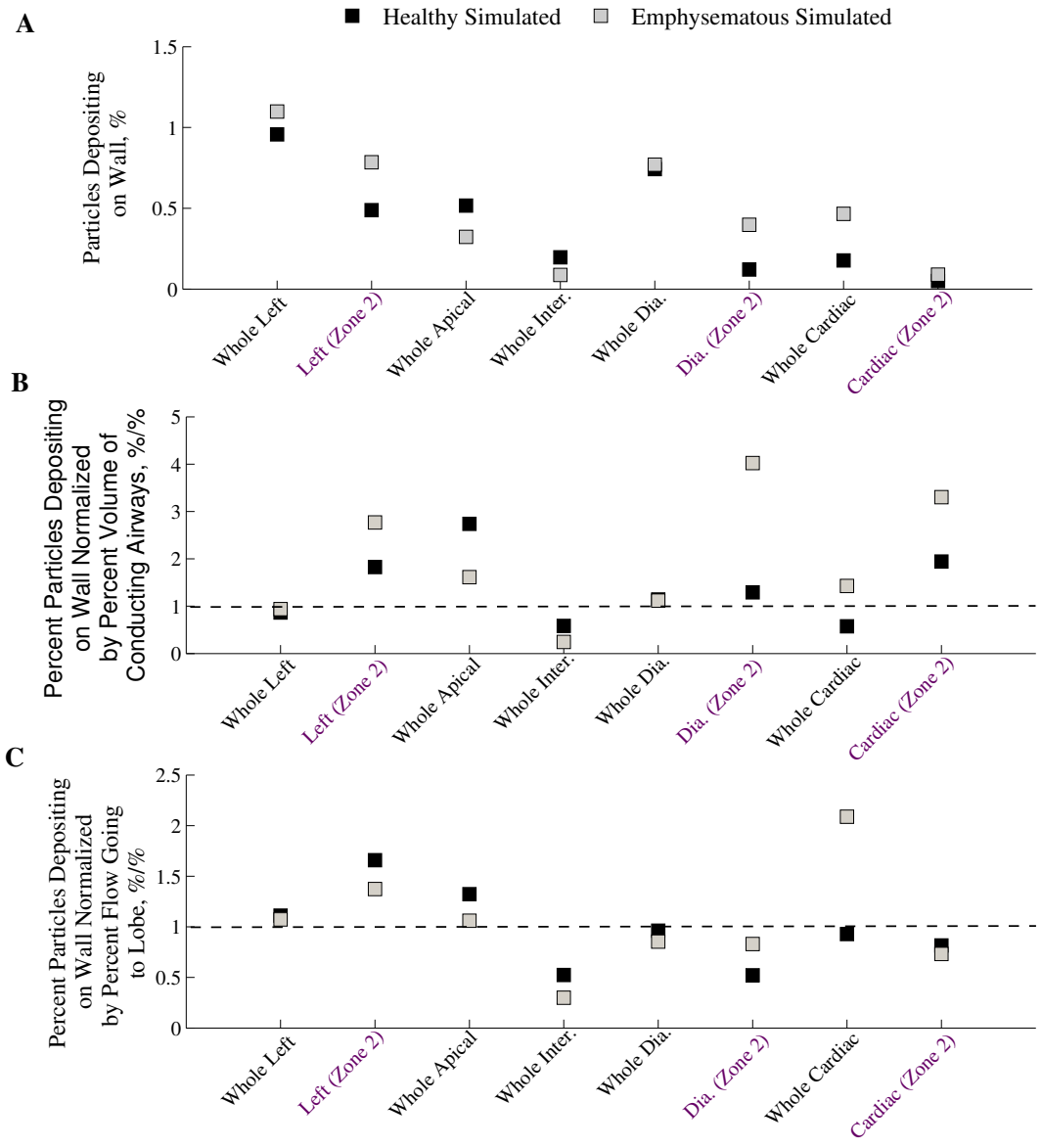

Figure 6: Panel A: Percent of particles depositing on each region of the 3D geometry, normalized by total number of particles simulated. Panel B: Percent of particles depositing on wall normalized by the volume of the conducting airways of each region. Panel C: Percent of particles depositing on wall, normalized by the number of particle depositing (Panel A), divided by the percent flow received by each region. Zone 2 only included the airways that led to only Zone 2, as defined in Figure 1B.

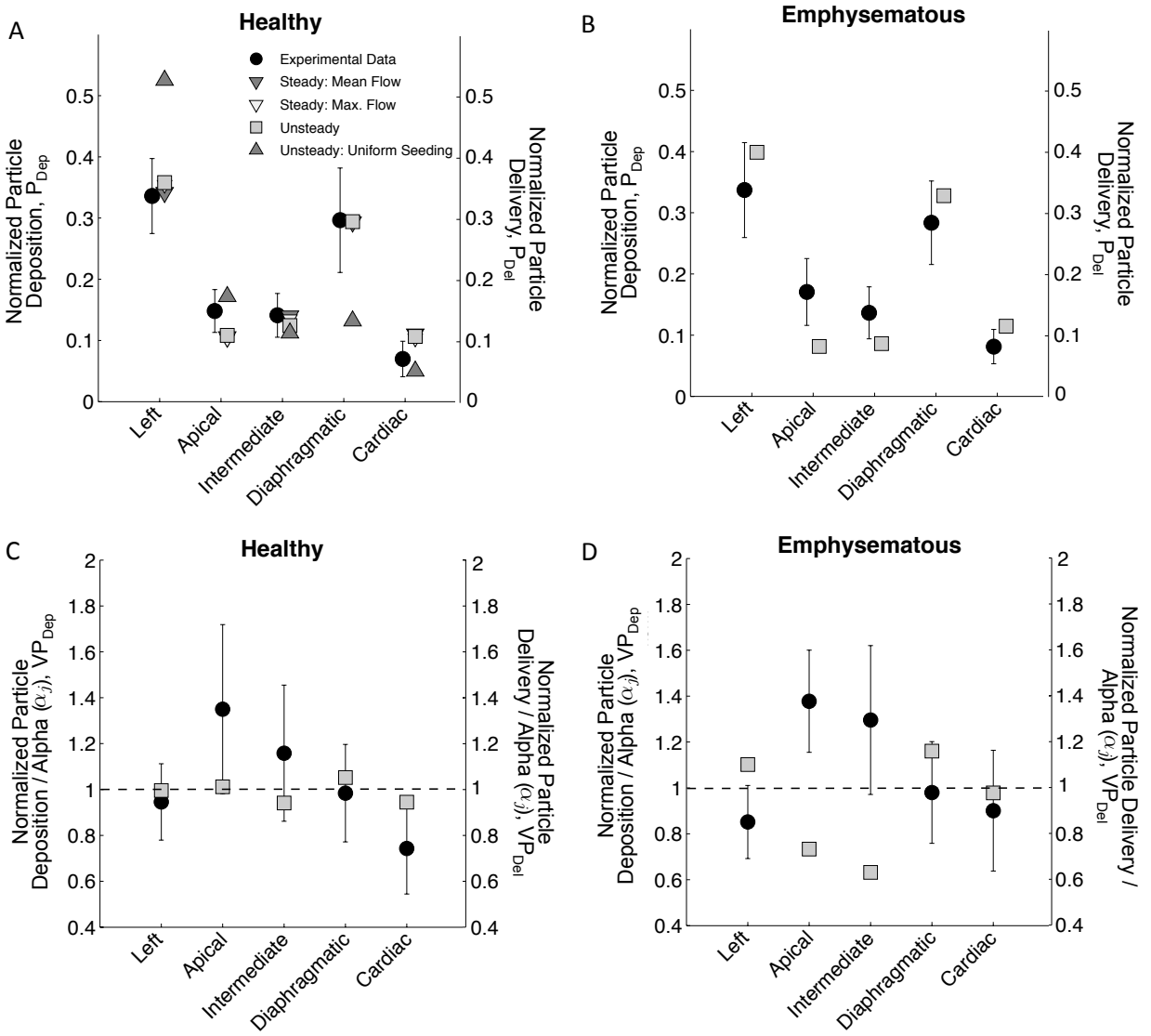

Figure 7: Panels A and B: Comparison of P_{Del} and P_{Dep} (20) for the healthy (uniform and parabolic seeding, panel A) and the emphysematous (panel B) rats. The particle delivery results for the steady simulations at mean and maximum inhalation flow rate are shown in panel A. Panels C and D: VP_{Dep} (20) and VP_{Del} for the 5 lobes of the healthy (panel C) and emphysematous (panel D) rat lungs. A value of 1 would indicate that deposition/particle delivery was proportional to the lobe volume.